Journal of Materials Chemistry

Cite this: *J. Mater. Chem.*, 2011, **21**, 17946

www.rsc.org/materials

PAPER

Pyrite nanocrystals: shape-controlled synthesis and tunable optical properties *via* reversible self-assembly†

Wei Li,[a] Markus Döblinger,[b] Aleksandar Vaneski,[c] Andrey L. Rogach,[c] Frank Jäckel*[a] and Jochen Feldmann[a]

Received 15th July 2011, Accepted 12th September 2011
DOI: 10.1039/c1jm13336e

Nanocrystals from non-toxic, earth abundant materials have recently received great interest for their potential large-scale application in photovoltaics and photocatalysis. Here, we report for the first time on the shape-controlled and scalable synthesis of phase-pure pyrite (FeS_2) nanocrystals employing the simple, inexpensive, thermal reaction of iron–oleylamine complexes with sulfur in oleylamine. Either dendritic nanocrystals (nanodendrites) or nanocubes are obtained by adjusting the iron-oleylamine concentration and thereby controlling the nucleus concentration and kinetics of the nanocrystal growth. Pyrite nanodendrites are reversibly assembled by washing with toluene and redispersed by adding the ligand oleylamine. The assembly–redispersion-process is accompanied by an increased absorption in the red/near-infrared spectral region for the aggregated state. This increased low-energy absorption is due to interactions between the closed-packed nanocrystals. High-concentration nanodendrite dispersions are used to prepare pyrite thin films with strong broadband extinction in the visible and near-infrared. These films are attractive candidates for light harvesting in all inorganic solar cells based on earth abundant, non-toxic materials as well as for photocatalytic applications.

Introduction

Colloidal semiconductor nanocrystals are currently considered as promising candidates for materials in photovoltaic and photocatalytic applications.[1–5] Their use in solar cells is motivated by the expectation of fusing the advantages of both inorganic bulk semiconductor and organic devices. In particular, one aims at larger charge carrier mobilities and smaller exciton binding energies as compared to organic materials while maintaining the advantages of simple and cheap solution processing. An additional advantage of nanocrystals is that with advanced colloidal chemistry the size and shape can be readily controlled which in turn governs important properties such as film formation and electronic coupling in thin films.[6–9] This has resulted in several reports on semiconductor nanocrystal-based all-inorganic[10,12] or hybrid,[13,14] *i.e.*, inorganic–organic, solar cells. However, most of the reported structures use either toxic or non-abundant materials such as Cd, Pb, In, *etc.* in at least one component. This means that, from a practical point of view, these materials cannot contribute significantly to a future sustainable energy supply. Instead, non-toxic, abundant, and thus cheap materials are much more promising and could make an impact even with overall lower efficiencies. Estimates of the annual electricity potential as well as material extraction costs recently led to the identification of materials that could be used in photovoltaic applications on a large scale.[15] Including the above-mentioned aspect of environmental friendliness, the most promising materials include iron and copper sulfide, copper oxides, and amorphous silicon.

While the above materials have extensively been studied, amongst others for photovoltaic applications, already in the 80s[16–20] the interest in their colloidal nanocrystal form is much more recent.[21–23] Solar cells employing copper sulfide and silicon nanocrystals have already been reported.[24,25] For iron sulfide, the large number of crystal phases[20,26,27] has complicated the synthesis of phase-pure colloidal nanomaterials. So far, phase-pure iron disulfide nanocrystals, with only few exceptions,[23,28–30] have been prepared with hydrothermal methods.[22,31,32] Shape-control, to the best of our knowledge, has only been reported in one occasion for a hydrothermal method based on different ligands and controlled concentrations of additives.[33] Hydrothermal approaches, however, employ high pressures and long reaction times frequently exceeding 10 hours and are not readily scalable.

Here, we report for the first time the simple, inexpensive, and scalable synthesis of phase-pure, shape controlled iron disulfide nanocrystals. Pyrite nanocrystals are obtained from a thermal

[a]*Photonics and Optoelectronics Group, Department of Physics and Center for NanoScience (CeNS), Ludwig-Maximilians-Universität München, Amalienstr. 54, 80799 Munich, Germany. E-mail: frank.jaeckel@physik.uni-muenchen.de*
[b]*Department of Chemistry, Ludwig-Maximilians-Universität München, Butenandtstr. 5-13 (E), 81377 Munich, Germany*
[c]*Department of Physics and Materials Science and Centre for Functional Photonics (CFP), City University of Hong Kong, Tat Chee Avenue, Kowloon, Hong Kong SAR*

† Electronic supplementary information (ESI) available: Fourier transformed infrared (FTIR) spectra of pyrite nanocrystal thin films and powders before and after sintering. See DOI: 10.1039/c1jm13336e

reaction of iron–oleylamine complexes with sulfur in oleylamine. Dendritic pyrite nanocrystals (nanodendrites) are obtained at a high iron precursor concentration while decreasing the iron precursor concentration leads to the formation of nanocubes. We attribute the shape control to different nucleus concentrations and thus different kinetics of the crystal growth. Furthermore, we demonstrate tunable optical properties of nanodendrite suspensions in the red and near-infrared spectral region *via* controlled and reversible aggregation and redispersion, which is mediated by the interaction between close packed nanocrystals. Finally, thin pyrite nanodendrite films are prepared and shown to exhibit promising optical properties for future photovoltaic and photocatalytic applications.

Experimental methods

Chemicals

$FeCl_2$ (anhydrous, 99.99%, Sigma-Aldrich), sulfur powder (99.998%, Sigma-Aldrich), oleylamine (OA) (80–90%, Acros), anhydrous ethanol (99.5%, Merck), toluene (99%, Merck). All chemicals were used as received.

Synthesis

We follow a general approach previously applied to other metal sulfides only (PbS, ZnS, CdS, and MnS).[34] $FeCl_2$ (51 mg/0.4 mmol or 254 mg/2 mmol for nanocubes or nanodendrites, respectively) was mixed with 6 mL OA in a three-neck flask and then reacted under a nitrogen atmosphere at 100 °C for 1 hour to form the Fe–OA complex. Afterwards, 6 mL OA solution of sulfur was quickly injected into the solution. The Fe/S-molar ratio was kept at 1/6. The resulting solution was heated to 220 °C and kept at this temperature for 20 min. After the solution was cooled to room temperature, 10 mL toluene was injected into the solution and 10 mL of ethanol was added to precipitate FeS_2 nanocrystals (NCs). The precipitate was further purified by washing with 1 : 1 toluene/ethanol mixture. Finally, FeS_2 nanocubes or nanodendrites were collected.

Reversible aggregation/dispersion and film preparation

The dispersion of the as-prepared FeS_2 NC aggregates into stable colloidal suspensions was achieved by adding OA. Typically, 50 μL of OA were added to 2 mL (30 mg mL^{-1}) of the aggregates in toluene, followed by simultaneous bath sonication and mild heating (~40 °C). Differently sized aggregates were obtained by different durations of the sonication treatment. During this procedure, the total mass per sample volume was kept constant. The obtained stable FeS_2 dispersions (30–100 mg mL^{-1}) were used as colloidal ink for spin coating onto clean glass substrates at 500–1000 rpm. The as-prepared films were sintered in a tube furnace at 350 °C for 1 h under Ar to remove solvents and OA. Washing with toluene allowed re-aggregation of the dispersed NCs which in turn could be redispersed using OA.

Characterization

The morphology of the samples was imaged with a scanning (SEM, Zeiss Ultra 55 Plus) and transmission electron microscope (TEM, JEOL JEM 1011, at 100 kV). High resolution TEM (HRTEM) and selected area electron diffraction (SAED) were carried out on a FEI Titan 80-300 microscope at 300 kV. For X-ray diffraction (XRD) analysis a Bruker D8 Discover diffractometer with Ni-filtered CuK-α-radiation was used. Dynamic light scattering (DLS) measurements were performed on a Zetasizer Nano S (Malvern Instruments, Malvern, UK). All solution measurements were carried out in toluene at 25 °C. The topographic and phase images of films were acquired simultaneously by atomic force microscope (AFM, JPK, NanoWizard). Absorption spectra of colloidal FeS_2 NC dispersions and FeS_2 NC films were recorded on a Cary 5000 UV-vis-NIR spectrophotometer. FeS_2 NC aggregates were investigated with an integrating sphere in Cary 500 UV-Vis-NIR spectrophotometer. This allowed for directly determining absorption and scattering contributions to the extinction.

Results and discussion

We first describe and discuss the shape control, structural characterization, and the growth mechanism of the pyrite nanocrystals, and then turn to the tunable optical properties in dispersions and thin films.

Shape control, structural characterization, and the growth mechanism

Fig. 1 displays representative scanning and transmission electron microscopy (SEM/TEM) images of the two different morphologies of pyrite nanocrystals obtained evidencing our first key result of efficient shape control within a simple synthesis. At a low iron precursor ($FeCl_2$) concentration of 0.4 mM we obtain only pyrite nanocubes (Fig. 1A and B) while under otherwise identical conditions a precursor concentration of 2 mM yields pyrite nanodendrites (Fig. 1D and E). The nanocubes have an average size of 150 nm while the nanodendrites have overall sizes around 40 nm and appear to consist of smaller particles of about 10 nm diameter as determined from TEM images (Fig. 1C and F).

The phase purity of the nanomaterials was evaluated at the local scale, *i.e.*, a few individual nanocrystals, from selected area electron diffraction (SAED), high resolution (HR) TEM, and at the bulk level from X-ray diffraction (XRD) patterns. Fig. 2A displays XRD patterns of nanodendrites and nanocubes. The observed patterns can be identified as reflections from lattice planes of cubic pyrite (JCPDS card no. 42-1340). Fig. 2B displays a HRTEM image of a single pyrite nanocube. Clearly visible is the single crystalline structure of the nanocube and individual lattice planes can be recognized. The lattice plane spacings of 0.54 nm and 0.27 nm correspond to the distances between (010) and (200) planes of cubic pyrite.[35] The reflections in the SAED pattern of an individual nanocube (inset Fig. 2B) can be assigned to the pyrite phase as well. We stress here, that in all three structural characterization methods, *i.e.*, SAED, HRTEM, and XRD, pyrite was found exclusively as crystal phase of iron sulfide demonstrating the high phase purity obtained here. Fig. 2C and D display the corresponding set of data for pyrite nanodendrites. Here as well, all structural features can be identified as originating from cubic pyrite: SAED and HRTEM only show spacings or reflections from pyrite lattice planes.

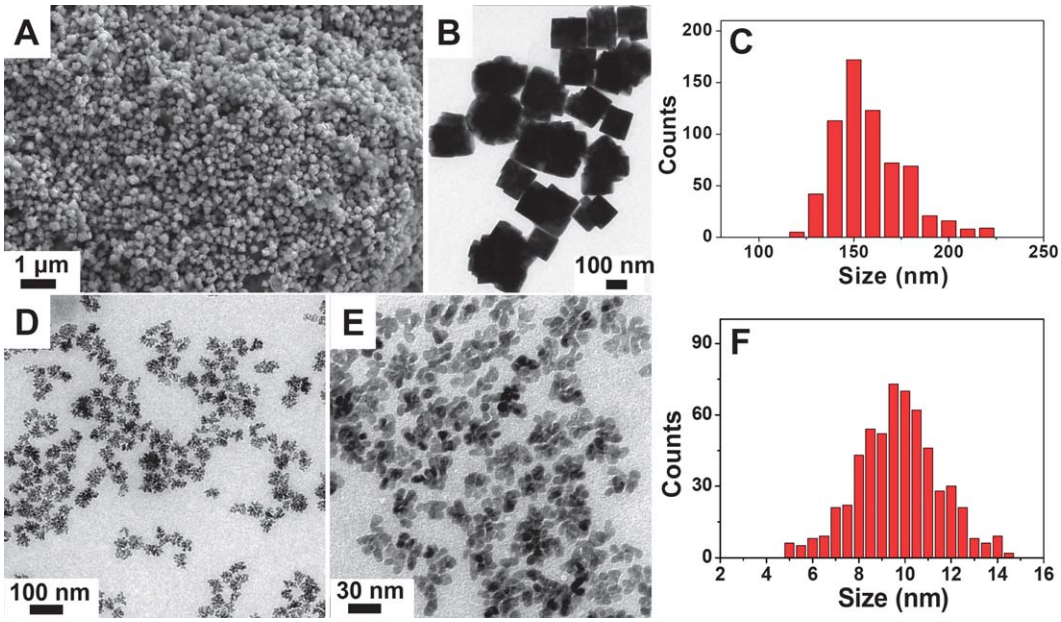

Fig. 1 SEM and TEM images of pyrite (A, B) nanocubes and (D, E) nanodendrites prepared *via* shape-controlled synthesis. Size distributions as determined from TEM images for nanocubes (C) and for subunits constituting the nanodendrite (F).

Also for the nanodendrites, no other crystal phase was detected. Interestingly, as evidenced from the HRTEM image in Fig. 2D, the individual smaller units constituting a nanodendrite have on the whole a fixed crystallographic orientation, *i.e.*, the same lattice planes in these subunits of an individual nanodendrite are parallel. We will discuss this observation with the growth mechanism below.

In order to obtain more insight into the growth mechanism, mixtures of iron–oleylamine complexes and sulfur were allowed to react for different durations and the resulting nanocrystals were investigated *via* TEM. Fig. 3A displays nanocubes obtained after 20, 60, and 180 min, respectively. For all these reaction times nanocubes are obtained, and their overall size increases. As evidenced from the temporal size evolution in Fig. 3C nanocubes grow from about 125 nm to almost 250 nm edge length. For nanodendrites we observe a faster growth, which practically terminates after 20 minutes (Fig. 3B and C). Two important observations can be made: first, at higher concentrations smaller, more anisotropic particles, *i.e.* nanodendrites are formed, and secondly, the growth proceeds faster at higher concentrations. Both observations point towards a nucleation and kinetically controlled growth mechanism as frequently observed in nanoparticle synthesis.[7,8,36–38] The general model is based on early studies of sulfur hydrogels formation and the accompanying theory,[39] *i.e.*, the LaMer-model: the fast injection of the precursor leads to a large degree of supersaturation in the growth solution which results in the formation of nuclei releasing the excess of free energy present in the system.[7] The nuclei formation in the growth solution reduces the degree of supersaturation and thus the precursor concentration below a critical value at which diffusion-dominated growth of the nuclei without further formation of new nuclei is observed. In the present case, as illustrated in Fig. 4, at a large precursor concentration a large number of nuclei can be formed by the process described above. This results in fast growth and overall smaller particles (Fig. 4B) since the distances between the nuclei that need to be overcome by diffusion are comparably small. In contrast, at a lower precursor concentration only few nuclei can be formed which then lead to a slower growth due to larger distances between the nuclei that need to be overcome by diffusion (Fig. 4A). At the same time, the resulting particles can be much larger. It is well documented in the literature that at high growth rates, *i.e.*, high precursor concentrations, kinetically controlled, anisotropic structures can be formed for both semiconductor and metal

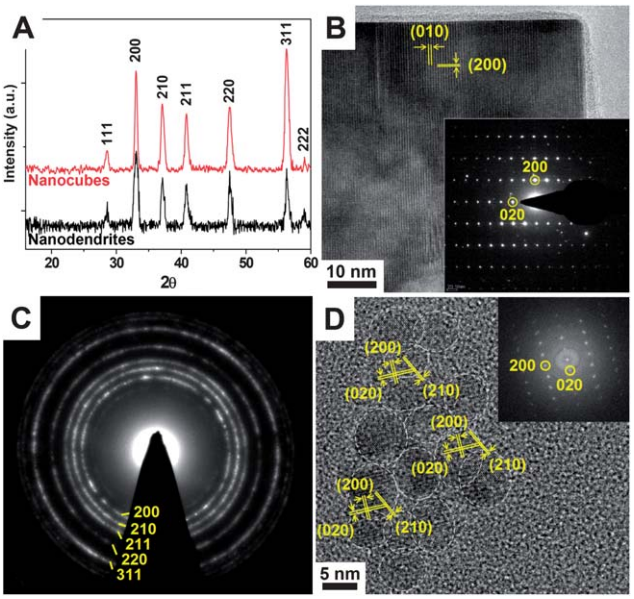

Fig. 2 (A) XRD patterns of pyrite nanocubes and nanodendrites. (B) HRTEM and SAED (inset) images of an individual pyrite nanocube. (C) SAED image from pyrite nanodendrites. (D) HRTEM with its fast Fourier transformed image (inset) of a whole individual pyrite nanodendrite. All images demonstrate phase-pure pyrite.

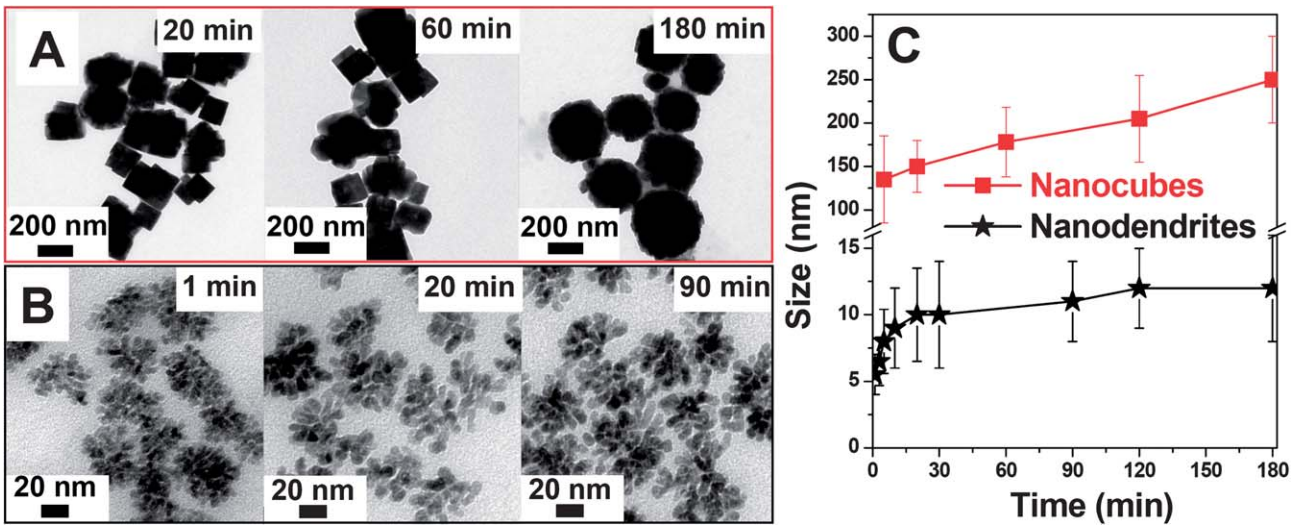

Fig. 3 TEM images of (A) pyrite nanocubes and (B) nanodendrites after different reaction times. (C) Evolution of nanocrystal size as function of reaction time for pyrite nanocubes (square) and subunits constituting nanodendrites (star) as determined from TEM images. Nanodendrites are smaller and grow faster than nanocubes.

nanoparticles.[7–11] Our above observation of the nanodendrite substructure (Fig. 2D) in which near-spherical crystallites are attached to each other with an overall single-crystal like orientation of their lattice planes and which occurs at faster growth rates supports such a kinetically controlled mechanism. The large number of fast growing nuclei will exhibit high-energy facets or facets with different ligand coverage. The high-energy or poorly covered facets then favor an oriented attachment, *i.e.* self-assembly, step of crystallites in which the overall free energy of the system is again minimized. Oriented attachment is a well-established, frequently observed process in the synthesis and structure formation of both metal and semiconductor nanoparticles.[40] During synthesis, it can occur spontaneously at large nuclei concentrations or it can be induced post-synthesis by destabilization of the ligand shell.[41,42] Next to interaction between crystal facets, dipole moments of the nanocrystals drive the oriented attachment process.[43–45] Following the oriented attachment step, the assembled crystallites continue growing. In contrast, at lower precursor concentrations and slower growth rates larger nanocubes are formed reminiscent of the cubic shape of bulk pyrite crystals. The suggested growth mechanism easily explains the shape-control as well as the lattice plane orientation of the pyrite nanocrystals.

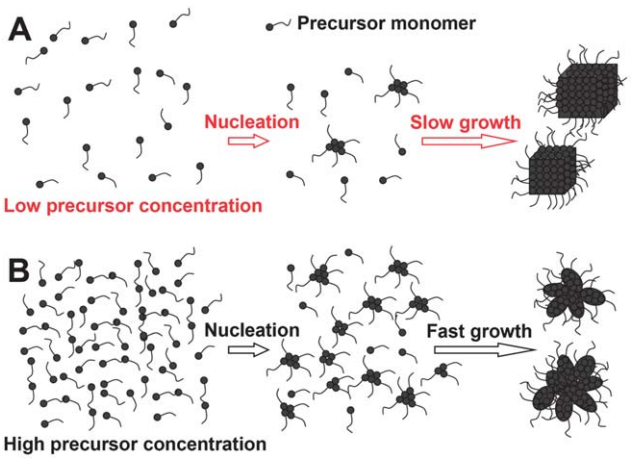

Fig. 4 Cartoon representation of the growth mechanism: (A) pyrite nanocubes are obtained at a low precursor concentration. The low concentration leads to a low nuclei concentration. The nuclei then grow slowly (diffusion limited) in quasi-equilibrium. (B) Nanodendrites are obtained at a high precursor concentration. The high concentration results in a high nuclei concentration. The nuclei then grow fast and kinetically controlled. Oriented attachment leads to the formation of nanodendrites.

Tunable optical properties of dispersions and thin films

Fig. 5A displays our second key result, the tunable optical properties of pyrite nanodendrites in dispersions. Well-dispersed nanodendrites in oleylamine display a broad extinction in the visible and near-infrared spectral region with larger extinctions at shorter wavelengths. Upon washing with toluene the extinction significantly increases for wavelengths longer than ~570 nm. This process is completely reversible by renewed addition of oleylamine. As evidenced by the TEM images and the size distributions from dynamic light scattering displayed in Fig. 5B, the increased extinction is caused by aggregation of the nanodendrites into higher order aggregates with increasing sizes up to almost 1 μm. The aggregation is caused by desorption of the ligands upon washing with toluene (see ESI† for related Fourier transformed infrared (FTIR) spectra). Since such large aggregates are expected to significantly scatter light we determined the pure absorption spectra of well-dispersed nanodendrites and the largest aggregates. As shown in Fig. 5C, the aggregation indeed induces new absorption bands in the red and near-infrared spectral range. Furthermore, close inspection (inset in Fig. 5C) reveals that the absorption onset is observed at an energy of about 0.9 eV (1370 nm). Pyrite nanocubes display stronger extinction at longer wavelength than nanodendrites (data not shown) due to larger scattering because of their larger size.

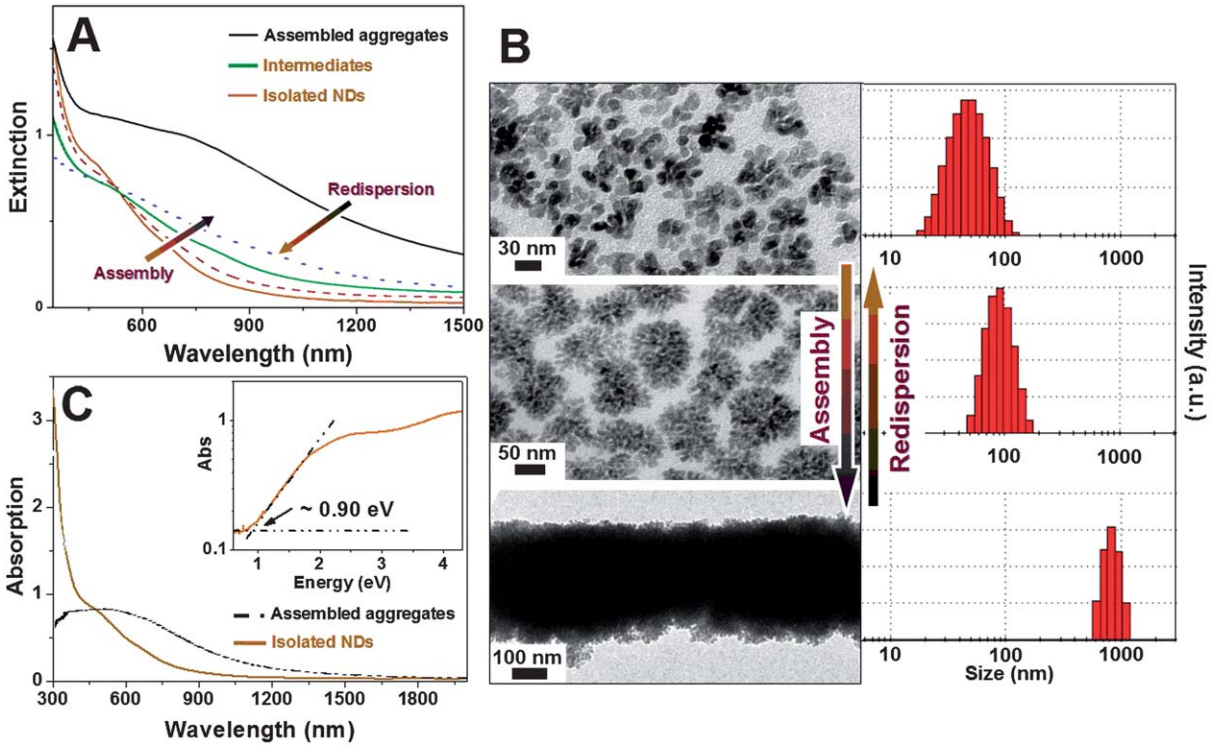

Fig. 5 (A) Reversible tuning of nanodendrite extinction spectra by washing with toluene (aggregation) and addition of oleylamine (redispersion), respectively. An increased absorption in the red/near-infrared spectral range is observed upon addition of toluene. (B) TEM images providing evidence that washing with toluene leads to formation of aggregates while addition of oleylamine leads to redispersion of the nanodendrites. Also shown are the corresponding size distributions as obtained from dynamic light scattering. (C) Absorption spectra of isolated and aggregated nanodendrites as obtained from integrating sphere measurements. The inset shows a semilogarithmic plot of the absorption onset region at ~0.9 eV.

The broad, slowly increasing absorption and extinction of well-dispersed pyrite nanodendrites reflects the indirect band gap nature of the material. The onset of the absorption at 0.9 eV corresponds to the indirect band gap found in bulk crystals of 0.8–1.2 eV.[28,46] The direct band gap at ~2.62 eV[47] is reflected in the extinction spectra by the increasing slope at wavelengths below 500 nm. We do not observe quantum size effects for the nanocrystals reported here. This is consistent with the fact that the exciton Bohr radius of pyrite is only ~1.3 nm.[28] The absence of quantum size effects excludes the possibility that the aggregation induced increased absorption in the red spectral range is due to wavefunction overlap of quantum confined carriers as observed in other systems.[48,49] However, the size of the constituting units of the nanodendrites is smaller than the electron mean free path in pyrite.[50] It has been shown that in superlattices of an indirect band gap material with a periodicity smaller than the electron mean free path, Brillouin zone folding and band mixing leads to quasi-direct transitions close to the indirect band gap.[51–54] Considering the present aggregates locally as supercrystals the increased absorption in the red could be understood as such quasi-direct transitions. In addition, the zone folding also modifies the phonon band structure,[55] which additionally may influence the transition probabilities for phonon-assisted indirect transitions. A similar phenomenon has recently been observed in

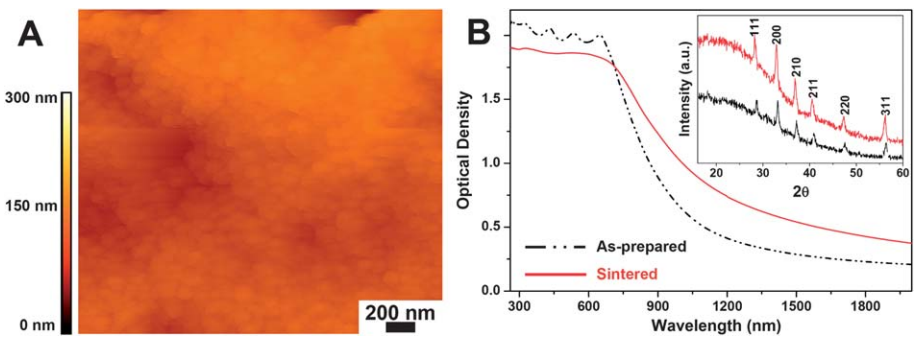

Fig. 6 (A) AFM topography image of a 600 nm thick thin film from pyrite nanodendrites. (B) Extinction spectra of the film before (dash dot dot) and after (solid) sintering. The inset shows the corresponding XRD pattern of the film.

copper sulfide nanocrystals and attributed to the same effect.[21] The increased absorption in the near-infrared region is an advantageous feature of this material with respect to light harvesting in photovoltaic applications.

As a first step towards photovoltaic applications, we prepared thin pyrite films from nanodendrites. Fig. 6A displays an AFM topography image of a 600 nm thick film. The films are comparably smooth with height variations of not more than 30 nm over micrometre distances. Pyrite nanocubes, in contrast, yielded much rougher films (roughness larger than 100 nm) and were therefore not investigated further for thin film preparation. Fig. 6B displays the optical extinction spectra of the thin film before and after sintering at 350 °C in an Ar atmosphere. Both films display broadband extinction in the visible and near-infrared which is very promising for light harvesting in photovoltaic or photocatalytic applications. The sintered film shows slightly higher extinction in the near-infrared region as compared to the as-prepared film. We attribute this to two effects: first, the removal of the ligand oleylamine (see ESI† for corresponding FTIR spectra) upon sintering will lead to increased absorption by the same mechanism that caused the increased absorption in the aggregates and, second, the sintered film has a higher degree of crystallinity as determined from the respective XRD patterns (inset in Fig. 6B), which may improve the absorption properties. Future work will explore the transport properties as well as performance of these films in all-inorganic solar cells.

Conclusions

In conclusion, we report the size and shape-controlled synthesis of pyrite nanocubes and nanodendrites *via* a simple, inexpensive, and scalable thermal reaction. Nanodendrites are obtained at a high precursor concentration that leads to a fast, kinetically controlled growth in which nanodendrites are formed in an oriented attachment step. Nanocubes are obtained at a low precursor concentration, which leads to a slower quasi-equilibrium growth resulting in comparably large particles. Nanodendrites display an absorption in the visible and near-infrared spectral range, which can be tuned reversibly through aggregation and redispersion of the nanoparticles in solution. Thin films from pyrite nanodendrites display a broadband extinction in the visible/near-infrared spectral range which is further improved through sintering. This renders pyrite nanocrystals promising materials for light harvesting in photovoltaic and photocatalytic applications.

Acknowledgements

We thank J. Szeifert, T. Bein, E. Wirnhier, W. Schnick, X. Kästele, and P. Klüfers for helpful discussions and support on experimental equipment. Financial support by the German Ministry for Education and Research (BMBF) through the cooperative project NanoPV and by the German Research Foundation (DFG) through the Nanosystems Initiative Munich (NIM) and LMU *excellent* is gratefully acknowledged.

Notes and references

1 P. V. Kamat, *J. Phys. Chem. C*, 2008, **112**, 18737.
2 K. Rajeshwar, N. R. de Tacconi and C. R. Chenthamarakshan, *Chem. Mater.*, 2001, **13**, 2765.
3 A. Kudo and Y. Miseki, *Chem. Soc. Rev.*, 2009, **38**, 253.
4 M. Berr, A. Vaneski, A. S. Susha, J. Rodríguez-Fernández, M. Döblinger, F. Jäckel, A. L. Rogach and J. Feldmann, *Appl. Phys. Lett.*, 2010, **97**, 093108.
5 A. Vaneski, A. S. Susha, J. Rodríguez-Fernández, M. Berr, F. Jäckel, J. Feldmann and A. L. Rogach, *Adv. Funct. Mater.*, 2011, **21**, 1547.
6 P. D. Cozzoli, T. Pellegrino and L. Manna, *Chem. Soc. Rev.*, 2006, **35**, 1195.
7 J. Park, J. Joo, S. G. Kwon, Y. Jang and T. Hyeon, *Angew. Chem., Int. Ed.*, 2007, **46**, 4630.
8 C. de Mello Donegá, P. Liljeroth and D. Vanmaekelbergh, *Small*, 2005, **1**, 1152.
9 D. V. Talapin, J.-S. Lee, M. V. Kovalenko and E. V. Shevchenko, *Chem. Rev.*, 2010, **110**, 389.
10 I. Gur, N. A. Fromer, M. L. Geier and A. P. Alivisatos, *Science*, 2005, **310**, 462.
11 X. Duan, X. Liu, Q. Chen, H. Li, J. Li, X. Hu, Y. Li, J. Ma and W. Zheng, *Dalton Trans.*, 2011, **40**, 1924.
12 J. M. Luther, M. Law, M. C. Beard, Q. Song, M. O. Reese, R. J. Ellingson and A. J. Nozik, *Nano Lett.*, 2008, **8**, 3488.
13 W. Huynh, J. Dittmer and A. P. Alivisatos, *Science*, 2002, **295**, 2425.
14 M. Law, L. E. Greene, J. C. Johnson, R. Saykally and P. Yang, *Nat. Mater.*, 2005, **4**, 455.
15 C. Wadia, A. P. Alivisatos and D. M. Kammen, *Environ. Sci. Technol.*, 2009, **43**, 2072.
16 G. Smestad, A. Ennaoui, S. Fiechter, H. Tributsch, W. K. Hofmann, M. Birkholz and W. Kautek, *Sol. Energy Mater.*, 1990, **20**, 149.
17 I. J. Ferrer and C. Sánchez, *Solid State Commun.*, 1992, **81**, 371.
18 A. M. Karguppikar and A. G. Vedeshwar, *Phys. Status Solidi A*, 1988, **109**, 549.
19 A. Ennaoui and H. Tributsch, *Sol. Energy Mater.*, 1986, **14**, 461.
20 A. Ennaoui, S. Fiechter, C. Pettenkofer, N. Alonso-Vante, K. Büker, M. Bronold, C. Höpfner and H. Tributsch, *Sol. Energy Mater. Sol. Cells*, 1993, **29**, 289.
21 I. Kriegel, J. Rodriguez-Fernandez, E. Da Como, A. A. Lutich, J. M. Szeifert and J. Feldmann, *Chem. Mater.*, 2011, **23**, 1830.
22 C. Wadia, Y. Wu, S. Gul, S. K. Volkman, J. Guo and A. P. Alivisatos, *Chem. Mater.*, 2009, **21**, 2568.
23 J. Puthussery, S. Seefeld, N. Berry, M. Gibbs and M. Law, *J. Am. Chem. Soc.*, 2011, **133**, 716.
24 Y. Wu, C. Wadia, W. Ma, B. Sadtler and A. P. Alivisatos, *Nano Lett.*, 2008, **8**, 2551.
25 C.-Y. Liu, Z. C. Holman and U. R. Kortshagen, *Nano Lett.*, 2009, **9**, 449.
26 K. Ramasamy, M. A. Malik, M. Helliwell, F. Tuna and P. O'Brien, *Inorg. Chem.*, 2010, **49**, 8495.
27 M. Akhtar, J. Akhter, M. A. Malik, P. O'Brien, F. Tuna, J. Rafteryand and M. Helliwell, *J. Mater. Chem.*, 2011, **21**, 9737.
28 J. P. Wilcoxon, P. P. Newcomer and G. A. Samara, *Solid State Commun.*, 1996, **98**, 581.
29 Y.-Y. Lin, D.-Y. Wang, H.-C. Yen, H.-L. Chen, C.-C. Chen, C.-M. Chen, C.-Y. Tang and C.-W. Chen, *Nanotechnology*, 2009, **20**, 405207.
30 P. V. Vanitha and P. O'Brien, *J. Am. Chem. Soc.*, 2008, **130**, 17256.
31 X. Chen, Z. Wang, X. Wang, J. Wan, J. Liu and Y. Qian, *Inorg. Chem.*, 2005, **44**, 951.
32 D.-W. Wang, Q.-H. Wang and T.-M. Wang, *CrystEngComm*, 2010, **12**, 755.
33 D. Wang, Q. Wang and T. Wang, *CrystEngComm*, 2010, **12**, 3797.
34 J. Joo, H. B. Na, T. Yu, J. H. Yu, Y. W. Kim, F. Wu, J. Z. Zhang and T. Hyeon, *J. Am. Chem. Soc.*, 2003, **125**, 11100.
35 Especially in the case of the large nanocubes, kinematically forbidden lattice planes or reflections like 010 are visible in the electron diffraction patterns.
36 A. B. D. Nandiyanto, F. Iskandar, T. Ogi and K. Okuyama, *Langmuir*, 2010, **26**, 12260.
37 Y. Wang, Y. Hu, Q. Zhang, J. Ge, Z. Lu, Y. Hou and Y. Yin, *Inorg. Chem.*, 2010, **49**, 6601.
38 K. X. Yao, X. M. Yin, T. H. Wang and H. C. Zeng, *J. Am. Chem. Soc.*, 2010, **132**, 6131.
39 V. K. LaMer and R. H. Dinegar, *J. Am. Chem. Soc.*, 1950, **72**, 4847.
40 Q. Zhang, S.-J. Liu and S.-H. Yu, *J. Mater. Chem.*, 2009, **19**, 191.
41 B. Lim and Y. Xia, *Angew. Chem., Int. Ed.*, 2011, **50**, 76.
42 Z. Tang, N. A. Kotov and M. Giersig, *Science*, 2002, **297**, 237.

43 Z. Tang, Z. Zhang, Y. Wang, S. C. Glotzer and N. A. Kotov, *Science*, 2006, **314**, 274.
44 Z. Zhang, Z. Tang, N. A. Kotov and S. C. Glotzer, *Nano Lett.*, 2007, **7**, 1670.
45 K.-S. Cho, D. V. Talapin, W. Gaschler and C. B. Murray, *J. Am. Chem. Soc.*, 2005, **127**, 7140.
46 I. J. Ferrer, D. M. Nevskaia, C. de las Heras and C. Sánchez, *Solid State Commun.*, 1990, **74**, 913.
47 A. K. Abass, Z. A. Ahmed and R. E. Tahir, *Phys. Status Solidi A*, 1986, **97**, 243.
48 J. Zhang, A. A. Lutich, A. S. Susha, M. Döblinger, C. Mauser, A. O. Govorov, A. L. Rogach, F. Jäckel and J. Feldmann, *J. Appl. Phys.*, 2010, **107**, 123516.
49 T. Vossmeyer, L. Katsikas, M. Giersig, I. G. Popovic, K. Diesner, A. Chemseddine, A. Eychmueller and H. Weller, *J. Phys. Chem.*, 1994, **98**, 7665.
50 A. M. Karguppikar and A. G. Vedeshwar, *Phys. Status Solidi A*, 1986, **95**, 717.
51 R. Tsu and L. Esaki, *Appl. Phys. Lett.*, 1971, **19**, 246.
52 P. A. Lebwohl and R. Tsu, *J. Appl. Phys.*, 1970, **41**, 2664.
53 U. Gnutzmann and K. Clausecker, *Appl. Phys.*, 1974, **3**, 9.
54 R. Zachai, K. Eberl, G. Abstreiter, E. Kasper and H. Kibbel, *Phys. Rev. Lett.*, 1990, **64**, 1055.
55 B. Jusserand, D. Paquet, A. Regreny and J. Kervarec, *Solid State Commun.*, 1983, **48**, 499.

